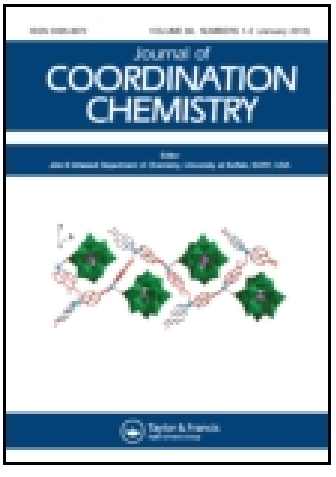

Journal of Coordination Chemistry
Publication details, including instructions for authors and subscription information:
http://www.tandfonline.com/loi/gcoo20

A comprehensive study on crystal structure, thermal behavior, and molecular dynamics of $[Sr(DMSO)_4(NO_3)_2]$

Natalia Górska[a], Elżbieta Szostak[a], Kacper Drużbicki[ab], Edward Mikuli[a], Akira Inaba[c] & Yasukazu Hirao[c]

[a] Faculty of Chemistry, Jagiellonian University, Kraków, Poland

[b] Frank Laboratory of Neutron Physics, The Joint Institute for Nuclear Research, Dubna, Russia

[c] Graduate School of Science, Osaka University, Toyonaka, Japan

Accepted author version posted online: 12 Sep 2014.Published online: 03 Oct 2014.

To cite this article: Natalia Górska, Elżbieta Szostak, Kacper Drużbicki, Edward Mikuli, Akira Inaba & Yasukazu Hirao (2014) A comprehensive study on crystal structure, thermal behavior, and molecular dynamics of $[Sr(DMSO)_4(NO_3)_2]$, Journal of Coordination Chemistry, 67:19, 3135-3154, DOI: 10.1080/00958972.2014.964225

To link to this article: http://dx.doi.org/10.1080/00958972.2014.964225

Journal of Coordination Chemistry, 2014
Vol. 67, No. 19, 3135–3154, http://dx.doi.org/10.1080/00958972.2014.964225

A comprehensive study on crystal structure, thermal behavior, and molecular dynamics of $[Sr(DMSO)_4(NO_3)_2]$

NATALIA GÓRSKA*†, ELŻBIETA SZOSTAK†, KACPER DRUŻBICKI†‡, EDWARD MIKULI†, AKIRA INABA§ and YASUKAZU HIRAO§

†Faculty of Chemistry, Jagiellonian University, Kraków, Poland
‡Frank Laboratory of Neutron Physics, The Joint Institute for Nuclear Research, Dubna, Russia
§Graduate School of Science, Osaka University, Toyonaka, Japan

(*Received 17 June 2014; accepted 21 August 2014*)

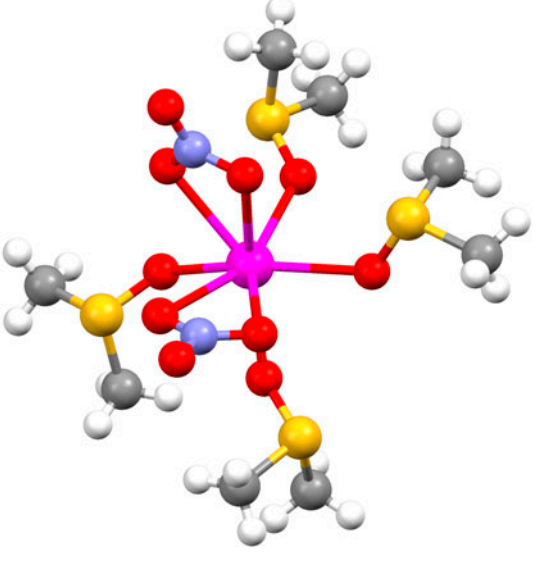

Three solid–solid phase transitions have been detected for $[Sr(OS(CH_3)_2)_4(NO_3)_2]$ at T^h_{C1} = 229.3 K, T^h_{C2} = 220.3 K, and T^h_{C3} = 171.6 K (on heating) and at T^c_{C1} = 226.6 K, T^c_{C2} = 219.1 K, and T^c_{C3} = 170.9 K (on cooling). The compound melts at $T_m \approx 347$ K. Thermal behavior of the deuterated analog is essentially the same, but the phase transitions' temperatures are shifted slightly towards higher temperature, by ca. 5, 5, and 15 K, respectively. Crystal structure in the lowest temperature of phase III at 93 K consists of completely ordered $(CH_3)_2SO$ molecules and bidentate nitrate groups, which are coordinated to strontium cation. Infrared (IR) spectra reveal that the phase transition at T^c_{C3} is associated with the slowing down of the reorientational motions of $(CH_3)_2SO$ and NO_3^- groups and also with the lowering of crystal lattice symmetry of the compound. The extended solid-state vibrational analysis has been performed for both deuterated and protonated

*Corresponding author. Email: gorska@chemia.uj.edu.pl

species by solid-state density functional theory computations and compared with IR and RS experimental spectra. Thermal decomposition occurs in two stages: in the first stage, in four steps, four $(CH_3)_2SO$ molecules are liberated and $Sr(NO_3)_2$ is formed, and in the second stage, above ca. 800 K, SrO is formed.

Keywords: $[Sr(DMSO)_4(NO_3)_2]$; Crystal structure; Phase transitions; Spectroscopic analysis; Solid state DFT

1. Introduction

Strontium is a nontoxic element even when it is administered in large doses for a prolonged period of time. It also appears to be one of the most effective substances found for the prevention and treatment of osteoporosis and other bone-related conditions [1–4]. Stable form of strontium (Sr^{2+}) when repeatedly administered can gradually eliminate radioactive strontium from the body by replacing it in bones. Radioactive strontium is excreted in the urine. Because of its chemical similarity to calcium, strontium can replace calcium to some extent in various biochemical processes in the body, including replacing a small proportion of the calcium in hydroxyapatite crystals of calcified tissues such as bones and teeth. Strontium in these crystals adds strength to these tissues. It also appears to draw extra calcium into bones. When rats or guinea pigs are fed with increased amounts of strontium, their bones and teeth became thicker and stronger [5–7].

Dimethyl sulfoxide, $[(CH_3)_2SO = DMSO]$, is also known for its various medical and biological applications in sports medicine, osteoarthritis, and anticancer activity [8–12]. Furthermore, it can be used as a drug carrier as it is also a nontoxic reagent which can easily penetrate through human skin [13].

We combined these two materials and formed a coordination compound with the formula, $[Sr(DMSO)_4(NO_3)_2]$. Among the compounds with DMSO ligands, it appeared to have an interesting structure with both DMSO and nitrate coordinated to the central metal. Previously investigated coordination compounds with a central metal also belonging to the second group of the periodic table, $[Mg(DMSO)_6](NO_3)_2$ [14] and $[Sr(DMSO)_6](ClO_4)_2$ [15], have different molecular structures (with all six DMSO molecules within coordination sphere), and are characterized by different polymorphism.

The general aim of the present study was to synthesize and characterize the crystal structure, thermal behavior and molecular dynamics of $[Sr(OS(CH_3)_2)_4(NO_3)_2]$ and its deuterated analog $[Sr(OS(CD_3)_2)_4(NO_3)_2]$ (hereafter referred to as SrHN and SrDN, respectively) in the wide temperature range using various physical methods like thermogravimetry (TG/SDTA), differential scanning calorimetry (DSC), X-ray single crystal diffraction (XRSCD), and vibrational spectroscopy (FT-IR and RS) supported by the state-of-the-art solid-state DFT computations.

2. Experimental

2.1. *Materials*

Two grams of anhydrous strontium nitrate was dissolved while being slowly heated to 330 K in 20 g of anhydrous $(CD_3)_2SO$ with 99.96% D atoms obtained from Sigma–Aldrich.

The solution was then chilled, and after a few hours, colorless crystals of [Sr(DMSO)$_4$(NO$_3$)$_2$] precipitated, were filtered, and dried over P_4O_{10} in a vacuum desiccator. The synthesized compound is highly hygroscopic so it was put in a sealed vessel and stored in a desiccator over P_4O_{10} as a desiccant. The protonated sample was synthesized analogically using dimethyl sulfoxide. The percent yields of the syntheses of deuterated and protonated products were 82 and 78%, respectively.

Before the measurements, the composition of the investigated compound was determined on the basis of carbon and hydrogen contents in DMSO ligand and nitrogen content in the NO_3 ligand from elemental analysis using a EURO EA 3000 instrument. Theoretical content for protonated sample [%]: C, 18.33; H, 4.62; N, 5.34. Found: C, 18.11; H, 4.82; N, 5.20. Theoretical content for deuterated sample [%]: C, 17.52; D, 8.82; N, 5.11. Found: C, 17.28; D, 9.03; N, 4.84.

2.2. *Methods*

TG/SDTA was conducted for [Sr(OS(CD$_3$)$_2$)$_4$(NO$_3$)$_2$] using a TG Mettler-Toledo 851^e instrument from 300 to 1100 K. The analysis was performed in a flow of high-purity argon (99.99%) with a constant heating rate equal to 10 K min^{-1}. The polycrystalline sample of [Sr(OS(CD$_3$)$_2$)$_4$(NO$_3$)$_2$] with a mass of 19.179 mg was measured in an open corundum crucible.

DSC measurements were obtained for both protonated and deuterated samples from 100 to 380 K using a Perkin-Elmer Diamond DSC calorimeter. The instrument was calibrated by melting of indium and water. The enthalpy changes (ΔH) linked up with observed

Table 1. Crystallographic data for [Sr(OS(CD$_3$)$_2$)$_4$(NO$_3$)$_2$] at 93 K.

CCDC	999875
Crystallographic method	Single-crystal diffraction
Diffractometer	Rigaku R-AXIS RAPID
Radiation	μ(MoKα) (λ = 0.71075 Å)
Empirical formula	C8D24N2O10S4Sr
Formula weight	548.30 g M^{-1}
Crystal size	0.3 × 0.3 × 0.1 mm^3
Temperature	93 K
Crystal system	Monoclinic
Space group	*C 2/c* (No. 15)
Unit cell dimensions	a = 17.4966(12) Å
	b = 9.4077(6) Å
	c = 13.8525(11) Å
	α, γ = 90°, β = 113.416(2)°
Volume	2092.4(3) Å^3
Z	4
D_{Calcd}	1.741 g cm^{-3}
F_{000}	1072
Absorption correction	Semi-empirical from equivalents
θ Range for data collect.	3.2°–27.46°
No of reflections collected	Total: 9723
	Unique: 2369 (R_{int} = 0.0671)
Absorption coefficient	3.020 mm^{-1}
Refinement method	Full-matrix least-squares on F^2
Data/restrains/parameters	2369/0/118
Goodness of fit on F^2	1.105
R indices (all data)	R_1 = 0.0599
	wR_2 = 0.1365

transitions were calculated by numerical integration of the DSC curves under the peaks of the anomalies. The entropy changes (ΔS) were calculated using the following formula: $\Delta S = \Delta H/T_C$.

XRSCD measurement was obtained for deuterated sample at 93 K using a Rigaku R-AXIS RAPID diffractometer with filtered Mo-Kα radiation and with a temperature accuracy of ± 2 K. The crystal-to-detector distance was 200.0 mm. The crystal is highly hygroscopic so it was protected with nujol during measurements. Details of the measurement and refinement are given in table 1. Full analysis of the crystal structure at 93 K was conducted by direct methods (SHELX-97 and SIR2004) [16, 17] using Yadokari-XG 2009 [18]. Crystallographic data have been deposited at the CCDC, 12 Union Road, Cambridge CB2 1EZ, UK. The deposition number is 999875.

FT-MIR spectra (4000–500 cm^{-1}) were performed at room temperature on a Jasco FT/IR-6100 spectrometer with a resolution of 2 cm^{-1} and 32 scans per each spectrum. The polycrystalline samples of protonated and deuterated compounds were suspended between KBr pellets. Additionally, temperature-dependent FT-MIR spectra were collected on a Bruker VERTEX 70v vacuum spectrometer for deuterated sample during cooling between 296 and 9 K. The polycrystalline sample was mixed with nujol and suspended between KBr pellets. The FT-FIR spectra (500–80 cm^{-1}) were collected at room temperature with the same instrument for protonated and deuterated samples, suspended in Apiezon N grease, and placed on a polyethylene disk. The spectra were collected with a resolution of 2 cm^{-1} and 64 scans per each spectrum.

Raman light scattering spectra were obtained at room temperature with a JASCO NR-1800 spectrometer from 4000 to 50 cm^{-1} and with a spectral resolution of 2 cm^{-1}. The incident radiation was $\lambda = 514.5$ nm.

Density functional theory (DFT) [19, 20] computations were applied in order to understand the vibrational properties of the quoted system. Periodic boundary conditions (PBC) and calculations were carried out using the plane-wave pseudopotential method and is implemented in CASTEP v6.0 [21, 22]. Exchange and correlation were defined using generalized gradient approximation (GGA) of the original PBE functional by Perdew [23, 24].

Designed nonlocal, norm-conserving pseudopotentials (NC) [25] were used along with the plane wave kinetic energy cut-off equal to 1050 eV (77 Ry). The size of the standard grid was set to 1.5, while 29.0517 $Å^{-1}$ was the maximum size of the *g*-vectors included. The Monkhorst-Pack grid was probed with the 2 × 2 × 1 accuracy. The fixed-cell geometry optimization was performed within the experimental cell parameters with the convergence criteria for the total energy, maximum force, maximum atomic displacement, and SCF iterations smaller than 5×10^{-7} $eVatom^{-1}$, 0.0025 $eVÅ^{-1}$, 5×10^{-5} Å, and 1×10^{-9} $eVatom^{-1}$, respectively.

3. Results and discussion

3.1. *Thermal analysis (TG/DTG/SDTA)*

The TG, DTG, and SDTA curves for $[Sr(OS(CD_3)_2)_4(NO_3)_2]$ are presented in figure 1. The sample is stable up to about 360 K. The thermal decomposition of the sample occurs in two main stages. From 360 to 530 K (stage I) it decomposes liberating all four DMSO ligands in four steps; 35.3% of the initial mass of the sample remains at 530 K and this value corresponds to percentage amount of strontium nitrate, which is stable up to ca. 800 K

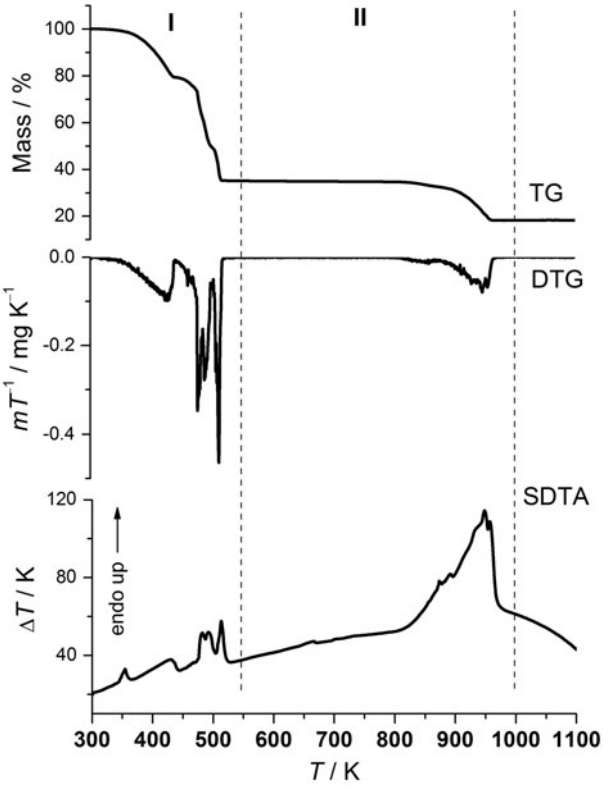

Figure 1. TG, DTG, and SDTA curves obtained for $[Sr(OS(CD_3)_2)_4(NO_3)_2]$ during heating at a constant rate of 10 K min^{-1}.

(stage II). In stage II, from 800 to 970 K, the resulting compound decomposes into strontium oxide; 18.3% of the initial mass of the sample remains after the second stage of thermal decomposition, and this corresponds well with the theoretical amount of SrO. The profile of the SDTA curve, which exhibits several endothermic maxima from 360 to 530 K and one broad maximum from 800 to 1000 K, also confirms the two stages of thermal decomposition. Another endothermic peak is visible at 354 K, which is associated with melting. Among coordination compounds with DMSO ligands and nitrate anions, thermal stabilities of $[Mg(DMSO)_6](NO_3)_2$ [14] and $[Al(DMSO)_6](NO_3)_3$ [26] have been investigated in argon. Decomposition of the magnesium compound starts at similar temperature (above 380 K) and occurs in three main stages. In the first stage, four DMSO molecules are liberated. The second stage is connected with the decomposition of resulting $[Mg(DMSO)_2](NO_3)_2$ and formation of solid mixture of $MgSO_4$, MgO, $Mg(NO_3)_2$, and other gaseous products of the DMSO and partial $Mg(NO_3)_2$ decomposition. In the third stage, the rest of the magnesium nitrate decomposes into oxygen, nitrogen oxides, and solid magnesium oxide. The final product of the decomposition at 840 K is a mixture of MgO and $MgSO_4$. Aluminum compound is slightly more stable and starts to decompose above 400 K. Its decomposition proceeds in one main stage from 400 to 550 K; 95% of the sample is decomposed. The final product of decomposition at 850 K is Al_2O_3.

3.2. *Phase transition investigations (DSC)*

The DSC measurements were carried out during heating and cooling of the two samples, SrHN and SrDN with masses of 14.064 and 15.681 mg, respectively. The applied constant rates were 5, 10, 30, and 50 K min^{-1}, between 100 and 380 K. Figure 2 shows the temperature dependences of the heat flow (three DSC curves) obtained during three subsequent runs: heating (curve No. 1), cooling (curve No. 2), and one more heating (curve No. 3) of the SrDN sample with a scanning rate of 40 K min^{-1}. There are three anomalies registered below room temperature: one sharp at 235.0 K, one broad at 227.1 K, and another sharp one at 187.4 K (during heating). These anomalies are connected with three solid–solid phase transitions. All transitions are accompanied by small thermal hysteresis of several degrees. While heating the sample above 300 K, one more distinct anomaly appears at T_m = 354 K, which is connected with melting. After cooling the liquid sample from 360 to 300 K, a sharp exothermic peak at 316 K can be observed, resulting from recrystallization. Figure 3 shows the comparison of the DSC curves obtained on heating and cooling of SrHN and SrDN samples with a scanning rate of 20 K min^{-1}. Shift of all three anomalies connected with the phase transitions in the solid state toward higher temperatures can be observed after deuteration with larger temperature differences for the transition at T_{C3}. The phase behavior of both compounds is essentially the same. Thermodynamic parameters of the detected phase transitions obtained for both compounds are presented in table 2. The phase transition temperatures were calculated by extrapolating corresponding dependences of T^h_{peak} and T^c_{peak} values *versus* the scanning rate equal to 0 K min^{-1}.

3.3. *Crystal structure in phase III (XRSCD)*

Table 1 presents experimental details of XRSCD of SrDN compound at 93 K (lowest-temperature phase III). We presented the results for SrDN sample because it was easier to grow a good-quality single crystal of this compound. The compound crystallizes in the

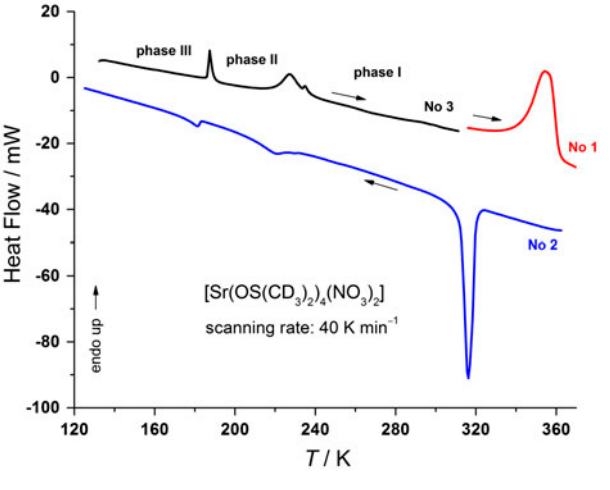

Figure 2. DSC curves obtained during subsequent heating (curve No. 1), cooling (curve No. 2), and heating (curve No. 3) of the $[Sr(OS(CD_3)_2)_4(NO_3)_2]$ sample.

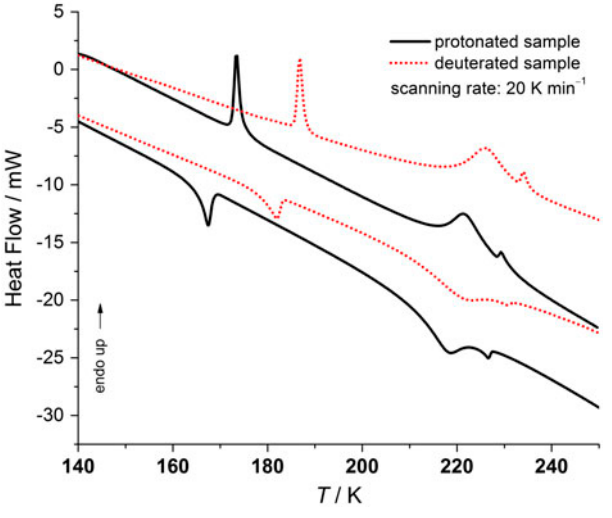

Figure 3. Comparison of the DSC curves obtained for [Sr(OS(CH$_3$)$_2$)$_4$(NO$_3$)$_2$] and [Sr(OS(CD$_3$)$_2$)$_4$)(NO$_3$)$_2$].

Table 2. Thermodynamic parameters of the detected phase transitions in protonated and deuterated forms of [Sr(DMSO)$_4$(NO$_3$)$_2$].

Parameters	[Sr(OS(CH$_3$)$_2$)$_4$(NO$_3$)$_2$] Heating	Cooling	[Sr(OS(CD$_3$)$_2$)$_4$(NO$_3$)$_2$] Heating	Cooling
T_m or T_{cr}/K	~347	~310	~355	~316
T_{C1}/K	229.3	226.6	234.0	230.8
T_{C2}/K	220.3	219.1	225.3	222.6
T_{C3}/K	171.6	170.9	186.3	183.0
ΔH_{1+2}/kJ M^{-1}	4.0	2.8	4.2	3.4
ΔH_3/kJ M^{-1}	1.2	1.1	1.2	1.2
ΔS_{1+2}/J M^{-1} K^{-1}	18.2	12.8	18.6	15.3
ΔS_3/J M^{-1} K^{-1}	7.0	6.4	6.4	6.6

monoclinic space group *C2/c* (No. 15) with $a = 17.497$ Å, $b = 9.408$ Å, $c = 13.853$ Å, and $\beta = 113.42°$ and $Z = 4$. Figure 4(a) and (b) presents the general view of the [Sr(OS(CD$_3$)$_2$)$_4$)(NO$_3$)$_2$] molecule and the unit cell packing.

Each Sr^{2+} is coordinated by four DMSO molecules through oxygens with Sr–O distances of 2.563 Å (*trans* position) and 2.504 Å (*cis* position), and four oxygens belonging to nitrates with Sr–O distances non-equivalent and equal to 2.679 and 2.663 Å. By coordination of nitrate, the complex achieves highly distorted octahedral geometry. All four DMSO molecules do not exhibit any dynamic disorder at this temperature. Detailed geometrical parameters with atomic coordinates and isotropic displacement parameters are listed in the Supplemental data (table S1, see online supplemental material at http://dx.doi.org/10.1080/00958972.2014.964225).

Table 3 also compares selected bond lengths and angles with the results of PBC, where the theoretical data refer to 0 K static computations. Some noticeable differences were

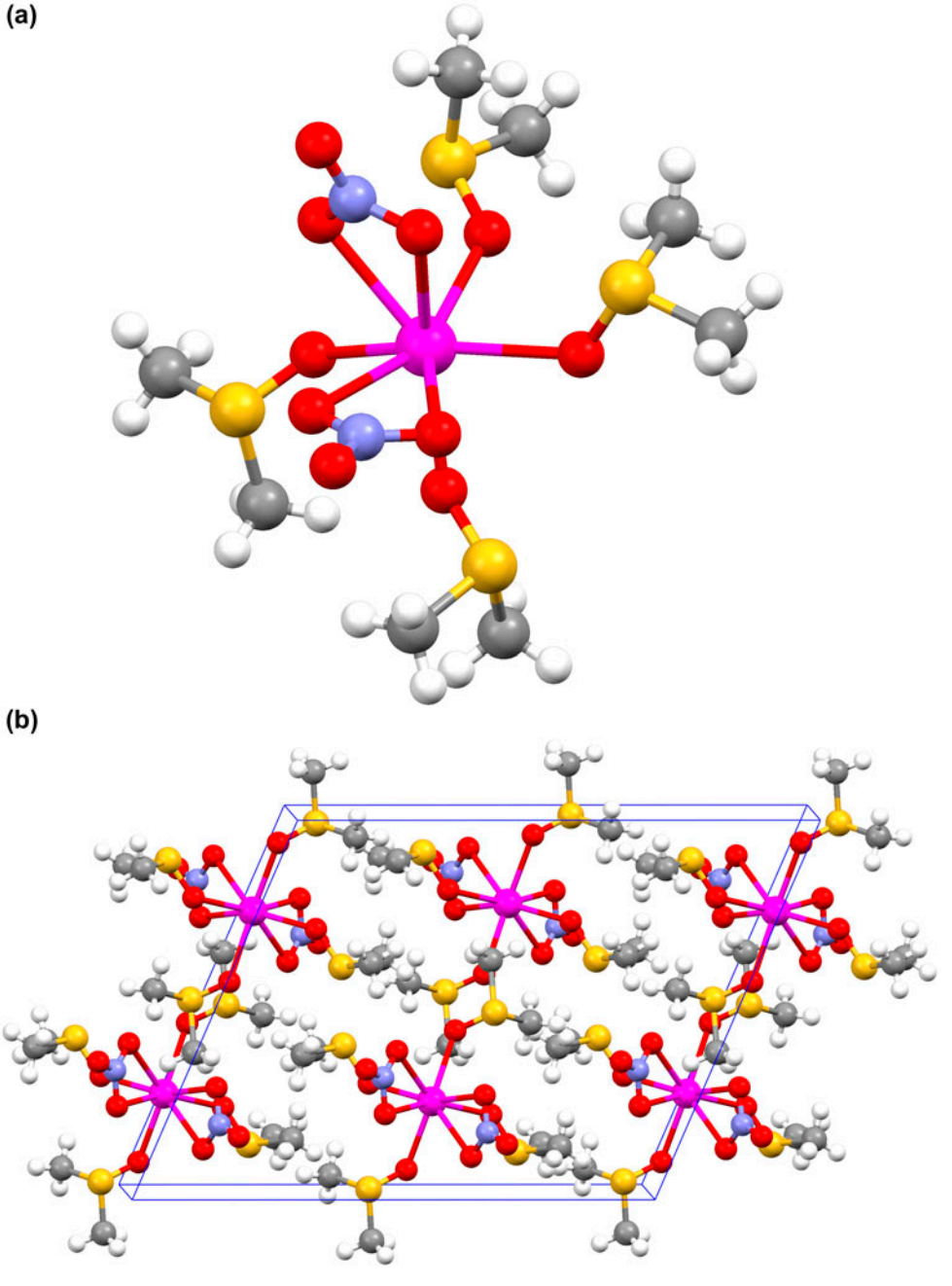

Figure 4. The general view of $[Sr(OS(CD_3)_2)_4(NO_3)_2]$ (a) and crystal structure at 93 K (b).

found in the case of bidentate O_2NO ions. However, the theoretical computations restored the related bond lengths and bond angles with an error smaller than 1% in most cases.

Table 3. Selected interatomic distances (Å) and angles (°) in $[Sr(OS(CD_3)_2)_4(NO_3)_2]$ determined from XRSCD at 93 K and computed by solid-state DFT at 0 K.

	XRSCD 93 K	DFT 0 K
Distances (Å)		
Sr(1)–O(1)	2.663(3)	2.6662
Sr(1)–O(2)	2.679(2)	2.6806
Sr(1)–O(4)	2.504(3)	2.5320
Sr(1)–O(5)	2.563(3)	2.5809
Sr(1)–N(1)	3.071(3)	3.0824
S(1)–O(4)	1.524(2)	1.5248
S(1)–C(1)	1.794(4)	1.8050
S(1)–C(2)	1.785(4)	1.8028
S(2)–O(5)	1.518(3)	1.5252
S(2)–C(3)	1.785(4)	1.8035
S(2)–C(4)	1.785(4)	1.7980
O(1)–N(1)	1.265(4)	1.2543
O(2)–N(1)	1.254(4)	1.2509
O(3)–N(1)	1.259(4)	1.2302
Angles (°)		
Sr(1)–O(4)–S(1)	132.40(15)	131.25
Sr(1)–O(5)–S(2)	123.74(13)	122.60
C(3)–S(2)–O(5)	106.28(19)	106.66
C(4)–S(2)–O(5)	106.37(19)	105.93
C(1)–S(1)–O(4)	106.29(17)	106.69
C(2)–S(1)–O(4)	105.19(15)	105.86
O(2)–N(1)–O(3)	121.1(3)	120.93
O(1)–N(1)–O(3)	119.6(3)	118.44
O(2)–N(1)–O(1)	119.3(3)	120.63
O(5)–Sr(1)–O(5)	148.07(12)	147.07
O(4)–Sr(1)–O(4)	115.26(12)	114.61

3.4. *Vibrational analysis*

3.4.1. Solid-state DFT computations of theoretical vibrational spectra. DFT computations were applied. The reported conventional *C2/c* unit cell solved at 93 K (a = 17.4966 Å, b = 9.4077 Å, c = 13.8525 Å, $\alpha = \gamma = 90°$, and β = 113.416°) was transformed by symmetry to the primitive one ($a = b$ = 9.9327 Å, c = 13.8525 Å, $\alpha = \beta$ = 110.48829°, and γ = 56.53271°), built of two molecules, reducing the system size by half. The lattice dynamic computations have also been repeated for the conventional cell, in order to ensure that the size reduction has no effect on the optical spectra, as observed.

The harmonic phonon frequencies at Γ point were obtained by diagonalization of dynamical matrices computed using density functional perturbation theory (DFPT) [27]. The linear response scheme was also used to compute the infrared (IR) activities of the crystal, while Raman activity tensors were calculated using a hybrid finite displacement/DFPT method according to Milman *et al.* [28] in the presence of an external field. For the frequencies computed at the zero wave vector the acoustic sum rule was imposed.

The calculated Raman activities (A_i) were finally transformed into the Raman intensities (I_i), using the relationship derived from the theory of Raman scattering [29]:

$$I_i = \frac{f(v_0 - v_i)^4 A_i}{v_i\left[1 - \exp\left(\frac{-hcv_i}{kT}\right)\right]} \quad (1)$$

where v_0 is the exciting wavenumber (in cm^{-1}); v_i is the frequency of the ith normal mode; h, c, and k are the fundamental constants; T is the temperature (298 K); and f is a suitably chosen common scaling factor for all the peak intensities. The resulting spectra presented here were uniformly broadened with Lorentzian line (with 8 cm^{-1} half-width). Analysis of the resulting eigenvectors was used in a tentative assignment of the computed modes, where the symmetry was labeled according to the IUPAC convention.

3.4.2. IR absorption and Raman scattering (RS) spectra. As the primitive unit cell consists of 98 atoms belonging to the *C2/c* (C_{2h}^5) space group, the 3 N phonon modes distribute over the irreducible representations as follows: $\Gamma_{red} = 74A_g + 74B_g + 74A_u + 74B_u$. The mutual exclusion rule results in ungerade A_u and B_u symmetry modes to be IR active, while, in contrast, gerade A_g and B_g ones are allowed in Raman spectroscopy. There are no silent modes present. While A_u and $2B_u$ modes are the acoustic ones, 291 modes are to be observed in optical vibrational spectroscopy.

The vibrational analysis of $[Mg(DMSO)_6]^{2+}$ complex of typical S_6 symmetry has been previously reported by Szostak, *et al*. [30], as well as the analysis of NO_3^- anions uncoordinated in some typical $[M(NH_3)_6](NO_3)_2$ and $[Ca(H_2O)_4](NO_3)_2$ systems [31, 32]. Here, we extend the vibrational analysis beyond the molecular modeling approach with PBC taking into account the crystal packing effects.

The data of full vibrational analysis of protonated and deuterated species are presented in table 4. According to the computations, the 75 lowest frequency vibrations are the lattice modes, while the remaining ones can be described as rather pure internal vibrations of the title complexes.

Figure 5(a) and (b) presents the experimental IR, Raman, and theoretical spectra obtained for both isotopic forms of the studied complex. An excellent general agreement between the experiment and theory has been achieved. Although deuteration does not change the symmetry of a particular phonon, it has very striking consequences on the force constants, resulting in the change of related wavenumbers and the vibrational amplitudes. Hence, it also strongly affects the related intensities. Moreover, it was clearly found that it also influences the coupling of modes and hence their nature, making proper band assignment a challenge.

3.4.2.1. *DMSO vibrations.* Despite the quasi-harmonic approximation, bands > 2000 cm^{-1} (νC–H/νC–D modes) are very well reproduced by theoretical calculations. Such an effect cannot be linked with any advantage of the used theory but rather with lucky cancelation of errors, known for GGA [33]. However, the computations clearly allow us to assign the recorded spectra. Two modes of B_u symmetry are dominating in the IR absorption spectroscopy, while two A_g modes are to be found by Raman spectroscopy. Both modes are separated by *ca.* 100 cm^{-1}, shifting to 750/780 cm^{-1} due to deuteration. The upper modes are linked with the asymmetric character, while the lower ones with the symmetric nature.

Towards the lower frequencies, the asymmetric methyl deformations $\delta_{as}(CH_3)$ are found at ~1440–1410 cm^{-1}. Upon deuteration, the frequencies fall to the range of ~1040–1000 cm^{-1}. In the protonated complex, these modes are strongly coupled with $\nu_{as}(NO_3^-)$ modes, which are excited at similar energies. The symmetric deformations $\delta_s(CH_3)$, which may be called *umbrella* modes, are found at ~1315–1250 cm^{-1}. In the case of deuterated system, the *umbrella* modes are much more mixed with the $\delta_{as}(CH_3)$ deformations, and there is no clear separation between these kinds of vibrations. The range 1030–900 cm^{-1} is

Table 4. The collection of $[Sr(DMSO)_4(NO_3)_2]$ optical phonon wavenumbers (in cm^{-1}) as observed experimentally at room temperature (IR, RS) and predicted by periodic DFT computations (CASTEP/PBE/NC-1050 eV). The tentative band assignment was based on the visualization of related eigenvectors. The symmetry representation of a given phonon is given in brackets.

Wavenumber (cm^{-1})/(symmetry)								
IR^{-H}	DFT^{-H}	RS^{-H}	DFT^{-H}	IR^{-D}	DFT^{-D}	RS^{-D}	DFT^{-D}	Tentative assignment
$[Sr(OS(CH_3)_2)_4(NO_3)_2]$				$[Sr(OS(CD_3)_2)_4(NO_3)_2]$				
3006	3071 (B_u)	2998	3083 (A_g)	2257	2278 (B_u)	2251	2285 (A_g)	ν_{as} (CH_3)/ν_{as}(CD_3)
2918	2962 (B_u)	2912	2964 (A_g)	2128	2120 (B_u)	2123	2120 (A_g)	ν_s (CH_3)/ν_s(CD_3)
1441	1433 (A_u)	1430	1423 (A_g)					δ_{as}(CH_3)
1423	1415 (B_u)	1415	1401 (B_g)					
1407	1343 (A_u)			1418	1352 (A_u)	1416	1355 (A_g)	ν_3,ν_4 = ν_{as}(O_2NO)/δ_{as}(CH_3) coupling
1386	1334 (B_u)			1385	1335 (B_u)	1403	1340 (B_g)	
1356	1280 (B_u)	1348	1307 (B_g)	1358	1281 (B_u)	1342	1301 (B_g)	
1334	1272 (A_u)	1318	1272 (B_g)	1328	1271 (A_u)	1319	1268 (A_g)	
1313	1270 (B_u)							δ_s(CH_3)
1294	1261 (B_u)	1297	1257 (A_g)					
				1053	1036 (B_u)	1054	1036 (A_g)	δ_{as}(CD_3)
		1041	1032 (A_g)			1040	1032 (A_g)	ν_1 = ν_s(O_2NO)
1028	1004 (B_u)							ρ(CH_3)
						1027	1004 (A_g)	δ_{as}(CD_3) + δ_s(CD_3)
				1026	992 (B_u)			δ_{as}(CD_3)
		1023	1003 (A_g)					ρ(CH_3)
				1009	972 (B_u)	1011	971 (A_g)	ν(S=O) + δ_s(CD_3)
960	945 (B_u)	961	947 (A_g)					ρ(CH_3) + ν(S=O)
938	921 (A_u)	938	921 (A_g)					ρ(CH_3)
904	891 (B_u)							
826	839 (B_u)			825	839 (B_u)	825	841 (A_g)	ν_2 = γ(O_2NO)
				781	814 (B_u)	779	814 (A_g)	ρ(CD_3) + ν(C–S)
				765	767 (B_u)	763	767 (A_g)	ρ(CD_3)
				726	744 (B_u)	726	744 (B_g)	ρ(CD_3)
725	739 (B_u)	725	740 (A_g)					ν_5 = δ(O_2NO)
711	685 (B_u)	712	692 (B_g)					ν_{as}(C–S)
						708	718 (A_g)	ν_6 = δ(O_2NO)
		680	662 (A_g)					ν_s(C–S)
						677	667 (B_g)	ρ(CD_3)
676	662 (B_u)							ν_s(C–S)
639	656 (B_u)							

(*Continued*)

Table 4. (*Continued*).

Wavenumber (cm^{-1})/(symmetry)								
IR^{-H}	DFT^{-H}	RS^{-H}	DFT^{-H}	IR^{-D}	DFT^{-D}	RS^{-D}	DFT^{-D}	Tentative assignment
				634	620 (A_u)	636	616 (A_g)	ν_{as}(C–S)
						623	606 (A_g)	ν_s(C–S)
		396	383 (A_g)					δ(C–S–C) + δ(O–S–C)/δ(S–O–Sr)
395	382 (B_u)							
				357	354 (A_u)			
						355	351 (A_g)	
						345	345 (A_g)	
				343	345 (B_u)			
		343	334 (A_g)					γ(S–O–Sr)
342	329 (A_u)							
						315	308 (A_g)	
314	303 (A_u)							δ(C–S–C)
		314	304 (A_g)					
313	305 (B_u)							
				270	260 (B_u)			
						269	264 (A_g)	
263	276 (B_u)							$\tau(CH_3)/\tau(CD_3)$
				200	198 (B_u)			
173	178 (A_u)			177	177 (A_u)			Lattice
133	136 (B_u)			165	170 (B_u)			Lattice
100	103 (A_u)			122	120 (B_u)			Lattice
70	88 (A_u)			99	101 (A_u)			Lattice

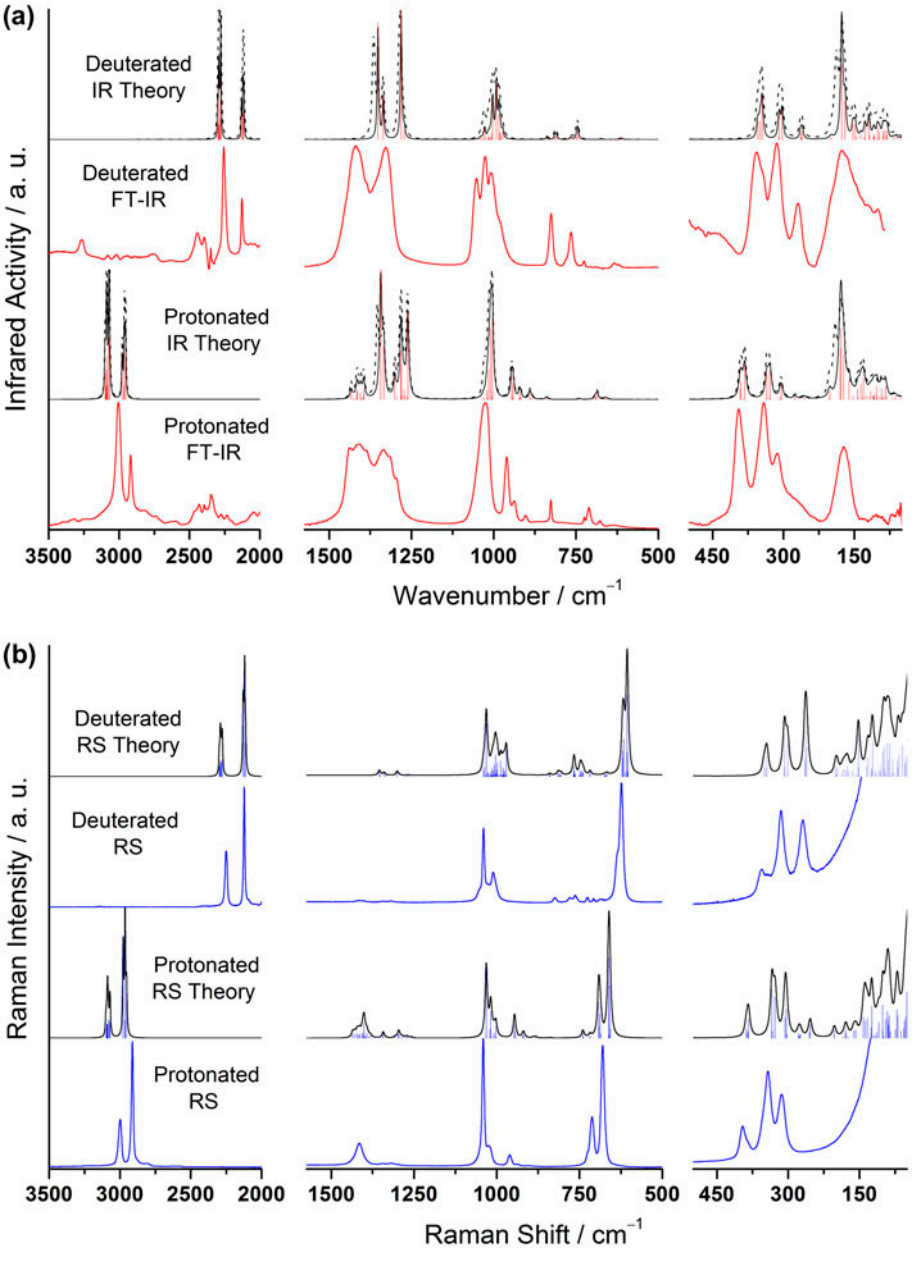

Figure 5. Comparison of experimental FT-IR (a) and Raman (b) spectra of deuterated and protonated forms of [Sr(DMSO)$_4$(NO$_3$)$_2$] with the corresponding theoretical spectra computed with plane-wave DFT using PBE/NC/1050 eV level of theory. The dotted lines in theoretical spectra denote the inclusion of the LO–TO splitting effect.

covered by the rocking $\rho(CH_3)$ modes which are coupled with the ν(S=O) modes located at 950 cm^{-1}. In the case of SrDN complex, the ν(S=O) stretching modes are likely coupled with the $\delta_s(CD_3)$ modes, as indicated in table 4. The rocking $\rho(CD_3)$ modes cover the range 830–660 cm^{-1}.

The decoupled asymmetric ν(C–S) modes can be observed in protonated sample at ~700 cm^{-1}, while the symmetric modes are at 680–640 cm^{-1}. In the case of the SrDN complex, these modes are at 635–605 cm^{-1}.

The bending deformation of the whole DMSO ligand (δ(C–S–C) + δ(O–S–C) coupled with the δ(Sr–O–S) are linked with the bands at ~395 cm^{-1} of the protonated sample. Upon deuteration, these modes are around 350 cm^{-1}. The out-of-plane γ(Sr–O–S) deformations are observed at ~340 cm^{-1}, while after deuteration at ~315 cm^{-1}. Finally, the δ(C–S–C) bending deformations may be found at ~315 and 270 cm^{-1} for the protonated and deuterated samples, respectively. The methyl torsional modes $\tau(CH_3)$ are observed in IR spectra of SrHN and SrDN samples at ~260 and 200 cm^{-1}, respectively.

3.4.2.2. *Bidentate O_2NO anions.* The free NO_3^- anion with D_{3h} symmetry has six normal vibrations of A_1', A_2'', and 2E′ symmetry. Two are doubly degenerated and therefore only four modes with different frequencies are observed. The first, $\nu_1 \equiv \nu_s(NO)A_1' \approx 1040$ cm^{-1}, is IR inactive and the second, $\nu_2 \equiv \gamma(NO_3)A_2''$ (out-of-plane) ≈ 830 cm^{-1}, is Raman inactive. The two modes with E' symmetry, $\nu_3 \equiv \nu_{as}(NO)E' \approx 1300$–$1400$ cm^{-1} and $\nu_4 \equiv \delta(ONO)E'$ (in-plane) ≈ 720 cm^{-1}, are active in both IR and Raman spectra [34]. The crystal structure and vibrational spectroscopy investigations indicated the presence of coordinated nitrate. When nitrate is monodentate or bidentate, then the symmetry lowers to C_{2v}, all bands become active, degeneracy of ν_3 and ν_4 is lifted, and shift of the bands may occur [35–40]. In fact, both the asymmetric stretching mode ν_3 and the in-plane bending mode ν_4 doubly degenerate in ionic nitrates with D_{3h} symmetry at *ca.* 1360 and 720 cm^{-1}, respectively, lose their degeneracy because of lowered symmetry (C_{2v}), and split into two components (ν_3 into ν_3 and ν_4, and ν_4 into ν_5 and ν_6) in IR spectra of SrHN and SrDN. Also, the symmetric stretching IR mode ν_1 forbidden in ionic nitrates becomes IR active. These features clearly eliminate the presence of ionic nitrates in the complexes studied here. Both coordinated monodentate (M–ONO_2) and bidentate (M–O_2NO) bonding give C_{2v} or C_s local site symmetry, depending on whether the nitrates are symmetric or not and exhibit similar splitting of the fundamental vibrational modes [41]. However, the magnitude of separation of ν_3 and ν_4 is larger for bidentate than for monodentate coordination if the complexes are similar. In our study, we observe the separation of two highest frequency bands of 80–100 cm^{-1}.

In our study, the asymmetric O_2NO modes were observed in the room-temperature IR spectra as broad bands covering the range ~1420–1330 cm^{-1} in both SrHN and SrDN compounds. The nature of this broadening may be quite interesting.

In order to interpret the related phonon modes, we rely on our computations. However, the plane-wave GGA computations have delivered relatively significant failure in the prediction of related wavenumbers, which are visibly underestimated, reaching *ca.* 60 cm^{-1} error. This fact may be mainly linked with some technical problems related to the use of relatively less accurate norm-conserving pseudopotentials (due to limitation of present implementation of linear-response approach), which may fail in such hypervalent configuration. It was also suggested by our background full electronic molecular-modeling computations that these modes are closer to the experimental values. However, the full electronic computations also do not clarify such broadening.

In general, the vibrational frequencies in both IR and Raman spectra can be influenced by coupling of the atomic vibrations with a macroscopic electric field. In such a situation, the IR-active modes have an associated dipole moment change that results in long-range dipole–dipole coupling. This coupling is always present in the IR spectra of crystalline

materials and manifests itself in a frequency difference between the longitudinal and transverse optical modes known as LO–TO splitting which is especially important for polar materials. For centro-symmetric structures, the mutual exclusion rule makes IR-active modes forbidden in Raman spectroscopy; hence, this effect is not expected in the Raman spectrum [42]. It was clearly demonstrated by Balan *et al.* [43] that LO–TO splitting may be an important factor influencing the observed IR spectra, and it should be included in computations. In our work, we have probed the influence of possible LO–TO splitting on the IR spectra of both species. In order to approximate the polycrystalline spectrum, the LO–TO splitting was calculated using the computed permittivity tensor and Born charges. The non-analytic contribution, which generates the LO–TO splitting, was added in the direction defined by the special points of the reciprocal space and the averaged IR spectrum was computed. According to our computations, such effect is indeed present in the studied case, splitting the A_u modes into the LO and TO components. Its value may be estimated as not greater than ~15 cm^{-1}, giving spectral broadening. Unfortunately, we were unable to observe the temperature dependence of this spectral range, due to overlapping with the nujol bands, but it is believed that such effects should also contribute significantly to the broadening.

The asymmetric $\nu_{as}(O_2NO)$ modes are visibly coupled with the $\delta_{as}(CH_3)$ deformations. Due to very low intensity, only the two lower bands can be detected in Raman spectroscopy, since the remaining ones are covered by the $\delta_{as}(CH_3)$ bands. However, upon deuteration, all the modes can be observed in the Raman spectrum. The bands are still significantly overlapped in related IR spectrum. The symmetric $\nu_s(O_2NO)$ modes are found in the Raman spectrum of both samples at ~1040 cm^{-1}. The out-of-plane $\gamma(O_2NO)$ deformations of the anions are observed in both SrHN and SrDN samples at ~826 cm^{-1}, while the in-plane $\delta(O_2NO)$ deformations are at 725 and 708 cm^{-1}, respectively.

3.4.2.3. *Lattice vibrations.* The range below 180 cm^{-1} is covered by optical lattice modes of a complicated nature. Figure 6 represents the visualization of the optical phonon modes of the deuterated system, as assigned to the most prominent experimental features in the FIR spectrum. The most prominent band at ~177 cm^{-1} (and predicted at the same wavenumber by theory) may be linked with the A_u symmetry mode, described as symmetric simultaneous stretching of all four Sr–O bidentate bonds. The B_u mode found as a shoulder at ~170 cm^{-1} may be defined as an asymmetric Sr–O stretch, where only one of the related bonds per anion is stretched. The B_u mode found and predicted at ~120 cm^{-1} may be defined as screwing of the DMSO molecules over the O–S bond. Finally, the lowest, A_u symmetry mode can be described as the screwing mode combined with a face-to-face wagging of the bidentate nitrates at each complex molecule. The terahertz range of the spectrum was not explored in our study.

3.4.3. IR spectra *versus* temperature (FT-IR). Figure 7(a) and (b) shows the IR spectra in two spectral ranges at 296–9 K for SrDN. The spectra marked with blue, red, and black were obtained in the high-, intermediate-, and low-temperature phases, respectively. Additionally, arrows indicate the phase transition temperatures. The assignment of the chosen IR bands to the corresponding phases was based on the DSC results obtained during cooling. For the transition at T_{C2} from phase II to phase I, mainly the band at 2257 associated with $\nu_{as}(CD_3)$ mode splits. Abrupt changes can also be observed for the transition at T_{C3} from phase III to phase II. Further splitting of the band at 2257 cm^{-1} occurs. Also, the bands at

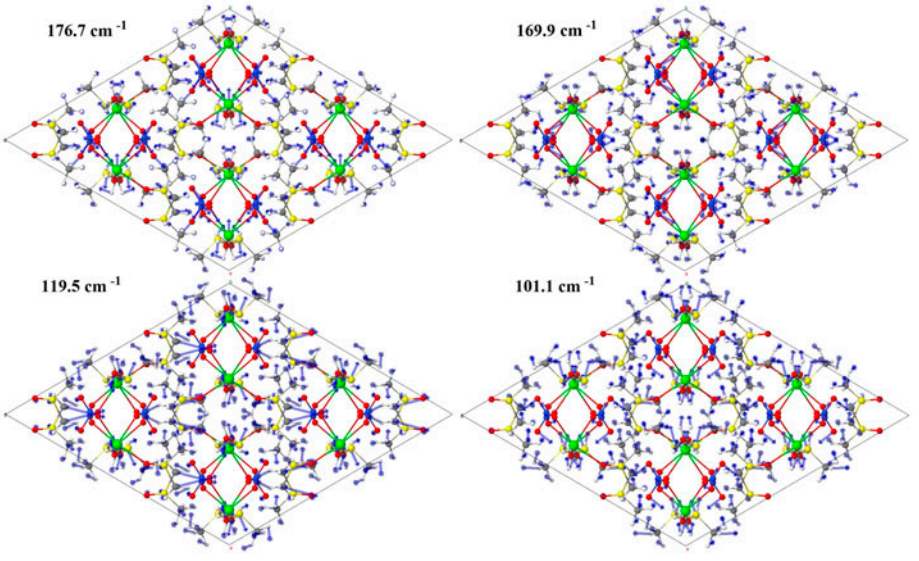

Figure 6. Exemplary visualization of the lattice modes (2 × 2 × 1 super cell) assigned to the experimental IR spectrum of the deuterated $[Sr(DMSO)_4(NO_3)_2]$ form based on periodic DFT computations (CASTEP/PBE/NC-1050 eV).

2128, 825, 781, and 765 cm^{-1} representing $\nu_s(CD_3)$, $\nu_2(O_2NO)$, and two $\rho_r(CD_3)$ modes, respectively, split into two components. These observations may indicate that the phase transitions at T_{C2} and T_{C3} are correlated with a reduction of symmetry in the $[Sr(DMSO)_4(NO_3)_2]$ crystal lattice.

To determine whether the observed phase transitions are correlated with changes in the reorientational dynamics of the methyl or nitrate groups, we followed the analysis of the full width at half maximum (FWHM) described by Carabatos-Nédelec and Becker, which is based on the theory used for the damping associated with an order–disorder mechanism [44]. The orientational correlation time, τ_R, is the mean time between instantaneous jumps from one potential well to another and is given by:

$$\tau_R = \tau_\infty \exp\left(\frac{E_a}{RT}\right) \tag{2}$$

where τ_∞ is the relaxation time at infinite temperature, E_a is the height of the potential barrier for CD_3 groups, and R is the gas constant. When $\bar{\omega}^2\tau_R{}^2 >> 1$ ($\bar{\omega}$ is the frequency of a particular mode) is the case here, the temperature dependence of the band width is described by [45]:

$$\mathrm{FWHM} = (a + bT) + c\exp\left(-\frac{E_a}{RT}\right) \tag{3}$$

where a, b, c, and E_a are the fitting parameters. The linear part of equation (2) corresponds to vibrational relaxation, and the exponential term corresponds to a diffuse thermal orientational mechanism (reorientational relaxation). We applied this analysis to the IR bands at 2128 and 825 cm^{-1}, associated with the $\nu_s(CD_3)$ and $\nu_2(O_2NO)$ vibrations. The peak

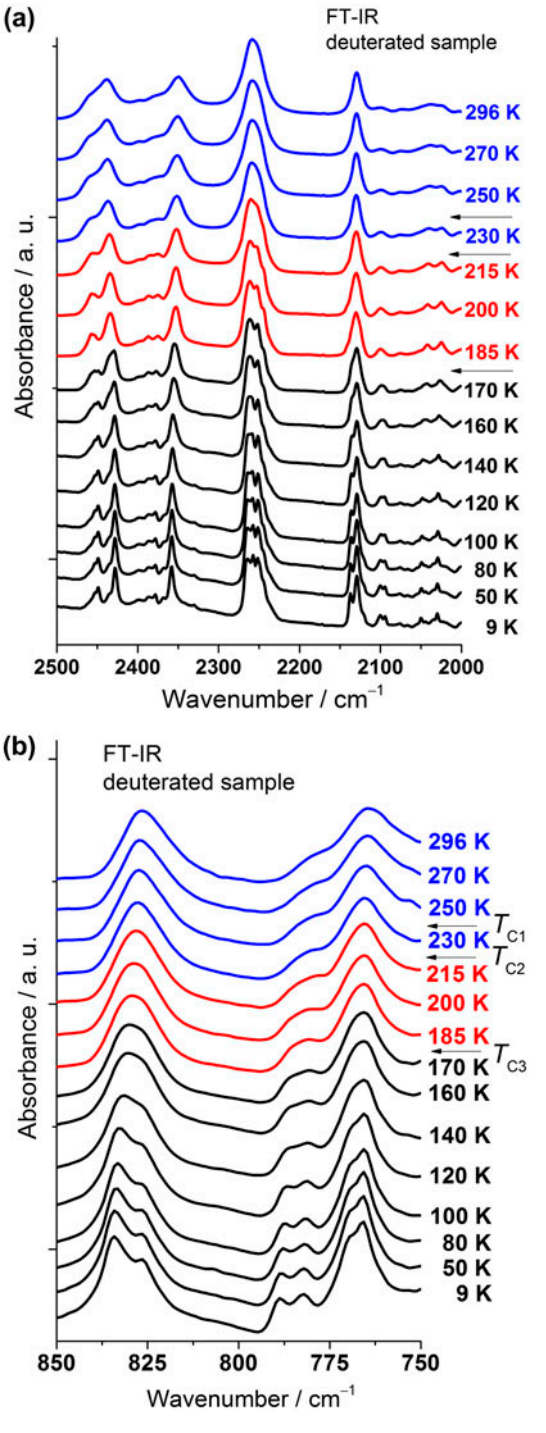

Figure 7. Temperature changes of IR spectra of $[Sr(OS(CD_3)_2)_4(NO_3)_2]$ in the temperature range of 296–9 K and in two spectral ranges: (a) 2500–2000 cm^{-1} and (b) 850–750 cm^{-1}.

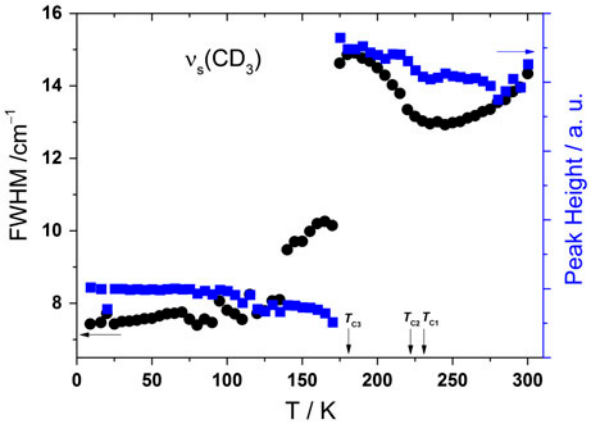

Figure 8. Temperature dependences of the FWHM and peak height of the IR band at 2128 cm^{-1} assigned to $\nu_s(CD_3)$ mode.

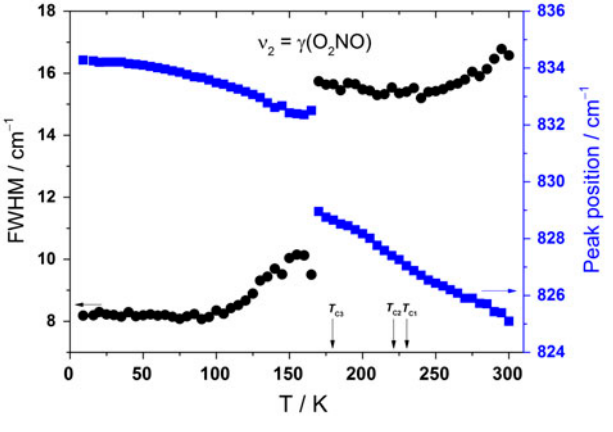

Figure 9. Temperature dependences of the FWHM and peak position of the IR band at 825 cm^{-1} assigned to $\nu_2(O_2NO)$ mode.

position and peak height of FWHM values at different temperatures were obtained by fitting with the Lorentz function. As both bands split below T_{C2}, deconvolution of these bands was applied.

Temperature dependences of the FWHM (marked with black circles) and peak height (marked with blue squares) of the IR band at 2128 cm^{-1} are plotted in figure 8. Reorientational motion of the methyl groups in phase I (above T_{C1}) and phase II ($T_{C1+C2} > T > T_{C3}$) is very fast (in the order of picoseconds). Subsequently, with lowering temperature below T_{C3}, the FWHM as well as the peak height decrease suddenly and become nearly constant at temperatures below 125 K. These behaviors indicate that the phase transition at T_{C3} is related to reorientation of the methyl groups. In phase III (below T_{C3}), only vibrational relaxation was observed.

Temperature dependences of FWHM (black circles) and peak position (blue squares) of the IR band at 825 cm^{-1} connected to out-of-plane bending vibration of nitrate groups ν_2(O_2NO) are presented in figure 9. The position of the band increases gradually, whereas the FWHM value decreases exponentially as the temperature decreases. A large drop of the FWHM value and distinct increase of peak position value can be observed at T_{C3}. The FWHM value becomes nearly constant below 100 K and is connected only with vibrational relaxation. Molecular dynamics of both DMSO molecules and O_2NO groups are clearly changed in the transition at T_{C3}. Similar spectroscopic study of the reorientational dynamics in another coordination compound with DMSO ligands: $[Mn(DMSO)_6](ClO_4)_2$ have also been reported [46].

4. Conclusions

(1) $[Sr(OS(CH_3)_2)_4(NO_3)_2]$ undergoes three solid–solid phase transitions at: T^h_{C1} = 229.3 K, T^h_{C2} = 220.3 K, and T^h_{C3} = 171.6 K (on heating) and at T^c_{C1} = 226.6 K, T^c_{C2} = 219.1 K, and T^c_{C3} = 170.9 K (on cooling). Deuteration shifts these phase transitions to higher temperatures: T^h_{C1} = 234.0 K, T^h_{C2} = 225.3 K, and T^h_{C3} = 186.3 K (on heating) and at T^c_{C1} = 230.8 K, T^c_{C2} = 222.6 K, and T^c_{C3} = 183.0 K (on cooling). Both compounds melt at $T_m \approx 347$ K and crystallize at $T_{cr} \approx 310$ K.

(2) The compounds decompose in two stages. In stage I, four DMSO molecules are liberated. Resulting $Sr(NO_3)_2$ is stable up to ca. 800 K and then decomposes into SrO in stage II.

(3) $[Sr(OS(CD_3)_2)_4(NO_3)_2]$ at 93 K belongs to monoclinic crystal system, space group *C2/c*, with a = 17.497 Å, b = 9.408 Å, c = 13.853 Å, and β = 113.42°. Each Sr^{2+} is coordinated by four oxygens from DMSO and four oxygens from bidentate nitrates. High- and intermediate-temperature phases I and II are probably highly orientationally disordered, whereas low-temperature phase III is completely ordered.

(4) Splitting of the $\nu_{as}(CD_3)$ IR band below T_{C2}, and $\nu_s(CD_3)$, $\rho_r(CD_3)$, and $\nu_2(O_2NO)$ IR bands below T_{C3} suggests lowering of the crystal symmetry at both phase transitions. Additionally, temperature dependences of the FWHM of IR bands at 2128 cm^{-1} [assigned to $\nu_s(CD_3)$] and at 825 cm^{-1} [assigned to $\nu_2(O_2NO)$] indicate that the reorientational motions of both methyl and nitrate are significantly slowed at T_{C3}.

(5) Harmonic vibrational frequencies, and related IR absorption, and Raman scattering intensities of protonated and deuterated forms of $[Sr(DMSO)_4(NO_3)_2]$ were determined using periodic DFT with PBE/NC/1050 eV level of theory calculated for a crystal. Excellent agreement was obtained between the observed and calculated frequencies.

Acknowledgements

This research was supported in part by PL-Grid Infrastructure. K. Drużbicki acknowledges the financial support of Polish Government Plenipotentiary for JINR in Dubna [grant number 118-8/1069-5/2014]. The research (FT-MIR, FT-FIR) was carried out with the equipment purchased, thanks to the financial support of the European Regional Development Fund in the framework of the Polish Innovation Economy Operational Program (contract no. POIG.02.01.00-12-023/08).

References

[1] S. Peng, X.S. Liu, S. Huang, Z. Li, H. Pan, W. Zhen, K.D.K. Luk, X.E. Guo, W.W. Lu. *Bone*, **49**, 1290 (2011).
[2] W. Qi, P. Wang, W. Guo, Y. Yan, Y. Zhang, W. Lei. *Biol. Trace Elem. Res.*, **143**, 302 (2011).
[3] M. Aranyosiova, M. Stancikova, J. Rovensky, D. Velic. *Surf. Interface Anal.*, **43**, 306 (2011).
[4] V. Geoffroy, D. Chappard, C. Marty, H. Libouban, A. Ostertag, A. Lalande, M.-C. de Vernejoul. *Osteoporos. Int.*, **22**, 289 (2011).
[5] S.C. Skoryna. *Can. Med. Assoc. J.*, **125**, 703 (1981).
[6] P.J. Marie, M.T. Garba, M. Hott, L. Miravet. *Miner. Electrolyte Metab.*, **11**, 5 (1985).
[7] M. Grynpas, P.J. Marie. *Bone*, **11**, 313 (1990).
[8] Z. Yu, P.J. Quinn. *Biosci. Rep.*, **14**, 259 (1994).
[9] D.L. Schrijvers. *Ann. Oncol.*, **14**, 26 (2003).
[10] L. Lebredo, R. Barrie, E.A. Woltering. *J. Surg. Res.*, **53**, 62 (1992).
[11] K. Wang, S.J. Adelstein, A.I. Kassis. *Appl. Radiat. Isotopes*, **66**, 50 (2008).
[12] M. Brindell, E. Kuliś, S.K.C. Elmroth, K. Urbańska, G. Stochel. *J. Med. Chem.*, **48**, 7298 (2005).
[13] D.C. Wood, J. Wood. *Ann. N. Y. Acad. Sci.*, **243**, 7 (1975).
[14] A. Migdał-Mikuli, N. Górska. *J. Therm. Anal. Calorim.*, **90**, 833 (2007).
[15] A. Migdał-Mikuli, E. Szostak, P. Bernard. *J. Therm. Anal. Calorim.*, **115**, 443 (2013).
[16] G.M. Sheldrick. *Acta Crystallogr. A*, 64, 112 (2008).
[17] M.C. Burla, R. Caliandro, M. Camalli, G.L. Cascarano, L. De Caro, C. Giacovazzo, G. Polidori, R. Spagna. *J. Appl. Crystallogr.*, **38**, 381 (2005).
[18] K. Wakita. *Yadokari-XG. Software for Crystal Structure Analyses, 2001. Release of Software (Yadokari-XG 2009) for Crystal Structure Analyses*; (b) C. Kabuto, S. Akine, T. Nemoto, E. Kwon. *J. Cryst. Soc. Jpn.*, **51**, 218 (2009).
[19] P. Hohenberg, W. Kohn. *Phys. Rev.*, **136**, B864 (1964).
[20] W. Kohn, L.J. Sham. *Phys. Rev.*, **140**, A1133 (1965).
[21] S.J. Clark, M.D. Segall, C.J. Pickard, P.J. Hasnip, M.J. Probert, K. Refson, M.C. Payne. *Z. Krist.*, **220**, 567 (2005).
[22] K. Refson, S.J. Clark, P.R. Tulip. *Phys. Rev. B*, **73**, 155114 (2006).
[23] J.P. Perdew, K. Burke, Y. Wang. *Phys. Rev. B.*, **54**, 16533 (1996).
[24] J.P. Perdew, K. Burke, M. Ernzerhof. *Phys. Rev. Lett.*, **77**, 3865 (1996).
[25] A.M. Rappe, K.M. Rabe, E. Kaxiras, J.D. Joannopoulos. *Phys. Rev. B*, **41**, 1227 (1990).
[26] N. Górska, A. Inaba, E. Szostak, E. Mikuli. *Thermochim. Acta*, **533**, 66 (2012).
[27] K. Refson, S.J. Clark, P.R. Tulip. *Phys. Rev. B.*, **73**, 155114 (2006).
[28] V. Milman, A. Perlov, K. Refson, S.J. Clark, J. Gavartin, B. Winkler. *J. Phys.: Condens. Matter*, **21**, 485404 (2009).
[29] G. Keresztury, S. Holly, G. Besenyei, J. Varga, A. Wang, J.R. Durig. *Spectrochim. Acta*, **49**, 2007 (1993).
[30] E. Szostak, K. Drużbicki, E. Mikuli. *J. Mol. Struc.*, **970**, 139 (2010).
[31] K. Drużbicki, E. Mikuli. *Spectrochim. Acta A*, **77**, 402 (2010).
[32] J. Hetmańczyk, Ł. Hetmańczyk, A. Migdał-Mikuli, E. Mikuli, K. Drużbicki, A. Wesełucha-Birczyńska, L.M. Proniewicz. *J. Chem. Phys.*, **131**, 094506 (2009).
[33] E. Balan, M. Lazzeri, S. Delattre, M. Méheut, K. Refson, B. Winkler. *Phys. Chem. Miner.*, **34**, 621 (2007).
[34] K. Nakamoto. *Infrared and Raman Spectra of Inorganic and Coordination Compounds*, 5th Edn, John Wiley & Sons, New York (1977).
[35] B.M. Gatehouse, S.E. Livingstone, R.S. Nyholm. *J. Chem. Soc.*, 4222 (1957).
[36] C.C. Addison, B.M. Gatehouse. *J. Chem. Soc.*, 613 (1960).
[37] G. Topping. *Spectrochim. Acta*, **21**, 1743 (1965).
[38] N.F. Curtis, Y.M. Curtis. *Inorg. Chem.*, **4**, 804 (1965).
[39] C.C. Addison, D.W. Amos, D. Sutton. *J. Chem. Soc. A – Inorg. Phys. Theor.*, **5**, 808 (1967).
[40] M. Choca, J.R. Ferraro, K. Nakamoto. *J. Chem. Soc., Dalton Trans.*, 2297 (1972).
[41] C.C. Addison, N. Logan, S.C. Wallwork, C.D. Garner. *Quart. Rev.*, **25**, 289 (1971).
[42] R. Durman, P. Favre, U.A. Jayasooriya, S.F.A. Kettle. *J. Cryst. Spec. Res.*, **17**, 431 (1987).
[43] E. Balan, M. Lazzeri, A.M. Saitta, T. Allard, Y. Fuchs, F. Mauri. *Am. Mineral.*, **90**, 50 (2005).
[44] C. Carabatos-Nédelec, P. Becker. *J. Raman Spectrosc.*, **28**, 663 (1997).
[45] G. Bator, R. Jakubas, J. Baran. *Vib. Spectrosc.*, **25**, 101 (2001).
[46] E. Szostak, A. Migdał-Mikuli, K. Hołderna-Natkaniec, R. Gwoździk-Bujakowski, A. Kaczor. *J. Coord. Chem.*, **65**, 2732 (2012).